# Anisotropic Heating and Cooling within Interplanetary Coronal Mass Ejection Sheath Plasma

Zubair I. Shaikh[1] , Daniel Verscharen[2] , Ivan Y. Vasko[3] , Bennett A. Maruca[4] , Dibyendu Chakrabarty[5] , and Anil N. Raghav[6] 

[1] Space Sciences Laboratory, University of California, Berkeley, 7 Gauss Way, CA 94720, USA; zubairshaikh584@gmail.com, zshaikh@berkeley.edu
[2] Mullard Space Science Laboratory, University College London, Holmbury St. Mary, Dorking, UK
[3] William B. Hanson Center for Space Sciences, University of Texas at Dallas, Richardson, TX, USA
[4] Department of Physics & Astronomy and Bartol Research Institute, 104 The Green, Newark, DE 19716, USA
[5] Space and Atmospheric Sciences Division, Physical Research Laboratory, Ahmedabad, India
[6] University Department of Physics, University of Mumbai, Santacruz (E), Mumbai-400098, India

## Abstract

This study presents the first comprehensive investigation of the relationship between heating and cooling, temperature anisotropy, turbulence level, and collisional age within interplanetary coronal mass ejection (ICME) sheaths, which are highly compressed, heated, and turbulent. Using Wind spacecraft data, we analyze 333 ICME sheaths observed at 1 au from 1995 to 2015. The proton temperature within the ICME sheaths has a log-normal probability distribution. Irrespective of instability growth rates, plasma unstable to proton-cyclotron (PC) and firehose instabilities appear to be statistically hotter, at least by a factor of 5 to 10, compared to stable plasma. We also observe relatively enhanced magnetic fluctuations and low collisional age, especially in regimes unstable to PC and firehose instabilities at low proton betas $\beta_p \lesssim 2$. In the case of high beta $\beta_p \gtrsim 2$, we observe high magnetic fluctuations close to the instabilities and less collisional age to the plasma unstable to firehose instability rather than near the mirror mode and PC threshold. Our findings suggest that heating processes dominate over cooling processes in producing proton temperature anisotropy in the ICME sheath region. Moreover, collisional age and magnetic fluctuations are critical in maintaining anisotropic and isotropic conditions.

*Unified Astronomy Thesaurus concepts:* Solar coronal mass ejections (310); Solar wind (1534); Interplanetary magnetic fields (824); Space plasmas (1544); Interplanetary turbulence (830); Collisional processes (2286)

## 1. Background and Motivation

Interplanetary coronal mass ejections (ICMEs) are large-scale magnetic field structures originating from the solar atmosphere and propagating through the heliosphere (D. F. Webb & T. A. Howard 2012; J. G. Luhmann et al. 2020). They are one of the main drivers of space weather and heliospheric disturbances (R. Schwenn 2006; V. Bothmer & I. A. Daglis 2007; E. Kilpua et al. 2017; A. Raghav et al. 2017; Z. I. Shaikh et al. 2018, 2019b; A. Raghav et al. 2023). Generally, an ICME exhibits three distinct regions: shock front, sheath, and magnetic cloud (T. H. Zurbuchen & I. G. Richardson 2006; Z. I. Shaikh & A. N. Raghav 2022; Z. I. Shaikh et al. 2023). The ICME sheath region is compressed, highly turbulent, and has a higher temperature than the ambient solar wind (e.g., E. Kilpua et al. 2017; Z. I. Shaikh et al. 2020). However, the underlying physical processes that heat the sheath plasma remain largely unknown. Several physical mechanisms have been suggested for the heating/cooling of ICME plasma, including (i) reconnection processes (N. A. Murphy et al. 2011), (ii) dissipation of Alfvén waves or turbulence (e.g., H. Li et al. 2017; E. Yordanova et al. 2021), and (iii) heating across collisionless shocks (K. Korreck et al. 2007). In this paper, we analyze how proton temperature anisotropy and associated kinetic plasma instabilities are related to other aspects of kinetic physics, such as collisional age, proton temperature, and fluctuations in the magnetic field.

As per the Chew–Goldberger–Low (CGL) relations, the flow of collisionless plasma in inhomogeneous magnetic field conditions can generate temperature anisotropy $T_{p\perp} \neq T_{p\parallel}$ (G. Chew et al. 1956; S. P. Gary 1993; D. Verscharen et al. 2019), where $T_{p\perp}$ and $T_{p\parallel}$ are temperatures perpendicular and parallel to the background magnetic field, respectively. In contrast, anisotropy-driven instabilities limit the anisotropy (S. P. Gary 1993; P. Hellinger et al. 2006; J. Kasper et al. 2008; P. H. Yoon 2017; D. Verscharen et al. 2019). In general, a useful technique for studying temperature anisotropy is to examine empirical fit relations between $R_p = T_{p\perp}/T_{p\parallel}$ and $\beta_{p\parallel} = 2\mu_0 N_p k_b T_{p\parallel}/B^2$, such as (P. Hellinger et al. 2006; B. A. Maruca et al. 2012; D. Verscharen et al. 2019)

$$R_p = 1 + \frac{a}{(\beta_{p\parallel} - \beta_0)^b}, \qquad (1)$$

where $a$, $b$, and $\beta_0$ are fit parameters. When $T_{p\perp} \neq T_{p\parallel}$ there exist at least four electromagnetic temperature anisotropy instabilities: mirror mode (MM), proton-cyclotron (PC), parallel firehose (PFH), and oblique firehose (OFH) instabilities (S. P. Gary 1993; P. Hellinger & H. Matsumoto 2000; P. Hellinger et al. 2006; P. H. Yoon 2017; D. Verscharen et al. 2019; J. Huang et al. 2020). The first two instabilities take place for $T_{p\perp} > T_{p\parallel}$ at all $\beta_{p\parallel}$, whereas the last two instabilities occur for $T_{p\parallel} > T_{p\perp}$ and $\beta_{p\parallel} \gtrsim 1$ (S. P. Gary 1993; J. C. Kasper et al. 2002; P. Hellinger et al. 2006; L. Matteini et al. 2007; B. Maruca et al. 2011; D. Verscharen et al. 2019). These instabilities generate electromagnetic fluctuations that cause the temperature anisotropy to decrease, returning the plasma to a state of marginal stability

(L. Matteini et al. 2006; P. Hellinger & P. M. Trávníček 2008; K. G. Klein & G. G. Howes 2015). Plotting parameter distributions in the $(R_p, \beta_{p\parallel})$ plane is a common technique to consider the contours of constant $\gamma$ (e.g., P. Hellinger et al. 2006). Instabilities are related to the maximum growth rate $\gamma$ (growth rate of its fastest-growing mode); i.e., $\gamma$ is never negative. This is because the $k = 0$ mode always produces a growth rate of zero since that mode is degenerate. This means that the $(\beta_{p\parallel}, R_p)$ plane is divided into two regions: one with $\gamma = 0$ (stable) and the other with $\gamma > 0$ (unstable) where the instability is active. Finding the exact boundary between these two regions is computationally tricky, so a small $\gamma$ value is typically chosen to serve as the "threshold", such as $\gamma = 10^{-4}\Omega_p$ and $\gamma = 10^{-3}\Omega_p$, etc. ($\Omega_p$ is the proton gyrofrequency; e.g., S. P. Gary 1993; P. H. Yoon 2017; D. Verscharen et al. 2019).

In the solar wind, proton temperature anisotropy is mostly constrained by the mirror instability and the PFH or OFH instabilities (S. P. Gary 1993; J. C. Kasper et al. 2002; P. Hellinger et al. 2006; S. D. Bale et al. 2009; B. Maruca et al. 2011; J. Seough et al. 2013; D. Verscharen et al. 2013; S. Shaaban et al. 2017; D. Verscharen et al. 2019; J. Huang et al. 2020). With increasing heliocentric distance, on average, both the slow and the fast wind approach the firehose instability (L. Matteini et al. 2007). B. A. Maruca et al. (2018) find that in Earth's magnetosheath, at high beta, the contours of constant growth rate are very similar for the PC and MM and the PFH and OFH instabilities. Moreover, the coupling of electrons and protons and of protons and alpha particles can affect the instability of the particles (B. A. Maruca et al. 2012; P. Yoon et al. 2019). Various mechanisms contribute to the heating and cooling processes, impacting the temperature anisotropy.

The CGL double-adiabatic expansion induces anisotropic cooling in which $T_{p\perp}$ decreases more quickly than $T_{p\parallel}$. On the other hand, perpendicular heating is linked to cyclotron-resonant absorption of Alfvén waves (e.g., S. R. Cranmer et al. 1999; P. A. Isenberg 2001; C.-Y. Tu & E. Marsch 2001; J. Kasper et al. 2008). Similarly, damping of kinetic Alfvén waves has been identified as a source of both perpendicular and parallel heating (F. Sahraoui et al. 2009; A. Schekochihin et al. 2009; B. D. Chandran et al. 2010; G. G. Howes 2010; F. Sahraoui et al. 2010). Important properties of the solar wind, such as the turbulent/fluctuating magnetic field amplitude, the proton temperature, and the collisional age, seem to be related to kinetic instabilities. These quantities are either increased or decreased close to the marginal stability thresholds (S. D. Bale et al. 2009; B. Maruca et al. 2011; K. Osman et al. 2012; P. Hellinger & P. M. Trávníček 2014; S. Vafin et al. 2019). S. D. Bale et al. (2009) demonstrates that collisionality significantly influences short-wavelength magnetic fluctuation power by relaxing temperature anisotropy away from instability conditions. P. H. Yoon (2016) suggests binary collisions may aid in the isotropization process, but they do not fully explain it. B. Maruca et al. (2011) suggest that the solar wind plasma unstable to mirror or firehose instability is around 3–4 times hotter than stable plasma.

Recently, Z. I. Shaikh et al. (2023) examined proton temperature anisotropy within the ICME sheath region and suggested that, like in the solar wind, MM and firehose instabilities mainly limit the anisotropy. It is an open problem to know the role of kinetic instabilities in basic kinetic plasma physics within the ICMEs. This study sheds light on the
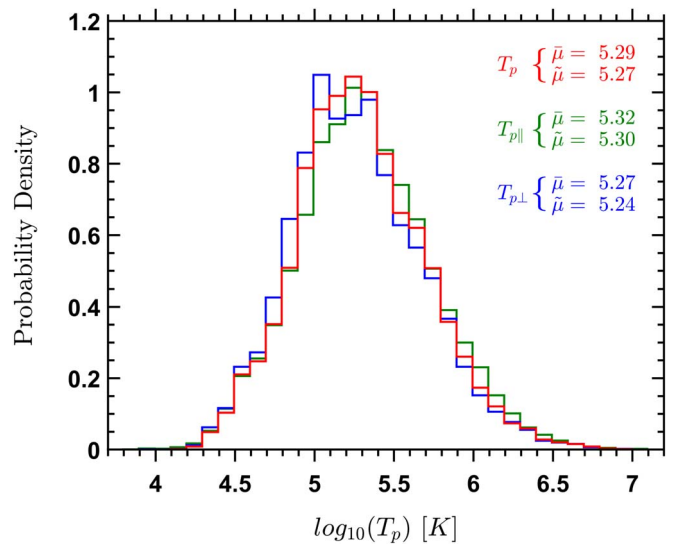


**Figure 1.** Probability density distribution of plasma proton temperature ($T_p$) and its components $T_{p\parallel}$ and $T_{p\perp}$ during all 333 ICME sheaths. We have also shown the mean ($\bar{\mu}$) and median ($\tilde{\mu}$) values.

relative roles of heating and cooling mechanisms in regulating temperature anisotropy within ICME sheaths at 1 au. Given the distinct characteristics of ICME sheath plasma, we aim to fill the gap through our investigation, providing insights into the interplay between heating/cooling processes, temperature anisotropy-driven instabilities, collisional age, and turbulence within ICME sheaths.

## 2. Analysis and Results

We examine 333 ICME[7] sheath regions observed from 1995 to 2015, which cover solar cycles 23 and 24. We analyze plasma and magnetic field data from the Solar Wind Experiment (SWE) and Magnetic Field Investigation (MFI) instruments on the Wind spacecraft (R. Lepping et al. 1995; K. Ogilvie et al. 1995).[8] Using a nonlinear least-squares fit of the data to a model assuming a bi-Maxwellian proton distribution function, the SWE provides 92 s time resolution proton density ($N_p$) and proton thermal speed ($V_{th}$) data, both parallel ($V_{th\parallel}$) and perpendicular ($V_{th\perp}$) to the magnetic field. Figure 1 shows the distribution of proton temperature ($T_p$) and its parallel ($T_{p\parallel}$) and perpendicular ($T_{p\perp}$) components for our 333 ICME sheath regions. We observe the log-normal probability distribution of temperature and its components, with the presence of a small hump on the right tail of the $T_{p\perp}$ distribution, which is reflected in the $T_p$ distribution as well. Compared to $T_p$ and $T_{p\parallel}$, we observed bifurcated peaks in $T_{p\perp}$, which is reflected in $T_p$ distribution at the relevant values. We do not observe significant differences in the mean ($\bar{\mu}$) and median ($\tilde{\mu}$) values of $T_p$, $T_{p\parallel}$, and $T_{p\perp}$. However, the average $T_{p\parallel}$ is slightly greater than the average $T_{p\perp}$.

To construct Figures 2–3, the $(\beta_{p\parallel}, R_p)$ parameter space is split into a grid of $100 \times 100$ logarithmically spaced bins. We eliminated those bins that had less than five data points. Figures 2 and 3 show the data distribution in the $(\beta_{p\parallel}, R_p)$ plane, where we observe that the distribution of $R_p$ narrows as $\beta_{p\parallel}$ increases. Here, the color bar shows the median value of

---

[7] wind.nasa.gov/ICME_catalog/ICME_catalog_viewer.php
[8] cdaweb.gsfc.nasa.gov/pub/data/wind/
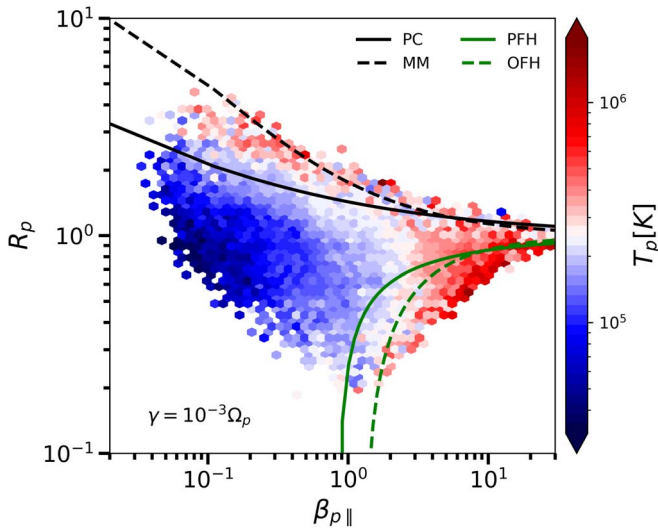
**Figure 2.** Distribution of $(\beta_{p\parallel}, R_p)$ for data points from the 333 ICME sheath regions from the Wind (1995–2015) spacecraft. The overplotted curves show thresholds for the PC, MM, OFH (dotted), and PFH instabilities with a maximum growth rate of $\gamma = 10^{-3}\Omega_p$. The color scale is the median value of $T_p$ in each bin. The highest median $T_p$ occurs in regions near or beyond the instability thresholds.

the respective plasma parameter in each bin. The overlaid curves in Figures 2 and 3 show thresholds for the PC, MM, PFH, and OFH instabilities derived using linear Vlasov–Maxwell theory by P. Hellinger et al. (2006) for $\gamma = 10^{-3}\Omega_p$ (see the Appendix for different growth rates). We observe that for $R_p > 1$, the MM instability threshold mainly constrains the $(\beta_{p\parallel}, R_p)$ distribution, whereas for $R_p < 1$, the OFH instability sets the more appropriate limit to the distribution. The data distribution is not strictly limited by the PC threshold, even at $\beta_{p\parallel} \leqslant 2$, where the PC has a lower threshold than the MM instability.

Figure 2 shows the median of $T_P$ over the $(\beta_{p\parallel}, R_p)$ plane. We observe a high $T_p$ value in regions where plasma is unstable to PC and PFH/OFH instability. Even at high $\beta_{p\parallel} > 2$, we observe high $T_p$ at the region close to $R_p = 1$, which is in contrast to solar wind at 1 au (B. Maruca et al. 2011). To determine which instability mostly affects the proton temperature within the ICME sheath, we plot the median $T_{p\parallel}$ and $T_{p\perp}$ in the $(\beta_{p\parallel}, R_p)$ plane in Figure 3. Comparing Figures 3(a) and (b) with Figure 2, we see that the enhanced $T_p$ near the plasma unstable to PFH/OFH instability threshold is largely due to an increase in $T_{p\parallel}$, whereas increased $T_p$ in the parameter unstable space to PC threshold region is mostly due to enhancement in $T_{p\perp}$. It may be worth mentioning the caveat that both $\beta_p$ and $R_p$ depend on temperature, so there are some trends baked into these plots. For example, temperatures generally increase with $\beta_p$ since $\beta_p$ is proportional to temperature. In the case of $\beta_{p\parallel} \leqslant 2$, we observed high temperature for anisotopic plasma with $R_p > 1$, whereas the median $T_p$ along bins of constant $\beta_{p\parallel}$ exhibits their minima at $R_p \sim 1$. In contrast, when $\beta_{p\parallel} \geqslant 2$, the $R_p$ dependence of $T_p$ along bins of constant $\beta_{p\parallel}$ ceases. Our result is consistent with the solar wind observation (B. Maruca et al. 2011). The plasma temperature unstable to PC and PFH/OFH instability is almost 5 to 10 times that of the neighboring stable plasma. The maximum enhancement in proton temperature is for the plasma unstable to the OFH threshold. For $\beta_{p\parallel} > 2$, we observe an enhancement in $T_{p\perp}$ even at the OFH instability threshold and regions located close to $R_p = 1$. Our

findings differ from the solar wind findings of B. Maruca et al. (2011), which show that solar wind plasma unstable to MM instability is around 3 to 4 times hotter than stable plasma. However, some of these differences may not be physical because these can be affected by bin size and threshold for the statistical significance of bins.

Figure 4(a) presents the median of collisional age $\tau = \nu_{pp}L/V_{sw}$ within each bin over $(\beta_{p\parallel}, R_p)$ plane, where $\nu_{pp}$ is the Coulomb proton–proton collision frequency, $L$ is distance of observed plasma parcel from the Sun (here it is 1 au), and $V_{sw}$ is the solar wind speed (see details in Appendix B). Thus, $L/V_{sw}$ is the transit time from the Sun to 1 au (S. D. Bale et al. 2009; P. Hellinger & P. M. Trávníček 2014). The $\tau$, also known as the "Coulomb number," is the number of collisions experienced by each proton during plasma expansion from the corona to 1 au. It assumes that the plasma parcel's density, velocity, and temperature remain fixed on its journey from the Sun to the observer. The plasma within the ICME sheath is relatively collisionless as $\tau \ll 1$. The low $\beta_{p\parallel} < 2$ intervals show high collisional age for $R_p \sim 1$, suggesting the higher the collision age, the more the system is isotropic. This is consistent with the solar wind (S. D. Bale et al. 2009; P. Hellinger & P. M. Trávníček 2014; S. Vafin et al. 2019). The collision age is small for high $R_p > 1$ (especially when unstable to PC instability). In the case of high $\beta_{p\parallel} > 2$, we observe a lower collisional age to the plasma unstable to OFH instability rather than near the MM and PC threshold. The collisional frequency exhibits a strong dependency on $T_p$, which is consistent with this trend (S. D. Bale et al. 2009; A. S. Richardson 2019). Moreover, plasma temperature and speed are dependent, suggesting that the higher $T_p$, the larger $V_p$. Thus, $\tau$ will get smaller where the temperature is higher, which is the case around OFH, according to Figure 3. In turn, the temperature is probably higher because of the OFH.

Figure 4(b) shows the median of the measured amplitude of the magnetic fluctuations $\delta B_{rms}/B_o$ per bin in the $(\beta_{p\parallel}, R_p)$ plane, where $\delta B_{rms}$ is a vector rms fluctuation estimated on the timescale of 92 s. $\delta B_{rms}/B_o$ is estimated at plasma temporal resolution (92 s) and during the largest scale (complete ICME sheath). We observe relatively low fluctuations in a region of low $\beta_{p\parallel} < 2$ and $T_{p\perp} < T_{p\parallel}$, whereas the amplitudes are higher when $T_{p\perp} > T_{p\parallel}$. We observe enhanced fluctuations in the case of high $\beta_{p\parallel} > 2$. Furthermore, the fluctuation amplitude is enhanced in the regions unstable to PC ($R_p \gtrsim 1$) and PFH/OFH ($R_p \lesssim 1$) instabilities and the region close to MM instability. MMs occur in spacecraft measurements, typically at much higher frequencies (shorter timescales) in the spacecraft frame (e.g., M. M. Ala-Lahti et al. 2018). Therefore, we consider their contribution to the measured rms fluctuations negligible. Moreover, the rms fluctuations are not limited to the compressive component alone. This suggests that MMs, while compressive, contribute only with a subdominant role overall. Near the instability thresholds, $\delta B_{rms}/B_o$ includes contributions from the fluctuations created by the instabilities themselves, but these are small compared to the background turbulence on those scales.

## 3. Discussion

ICME sheath plasma, characterized by high turbulence levels and enhanced temperatures compared to the surrounding solar wind, has been a subject of intense research (E. Kilpua et al. 2017; Z. I. Shaikh et al. 2020). Our investigation of 333 ICME sheaths using Wind observations shows the distribution of $R_p$ becomes narrower as plasma beta $\beta_{p\parallel}$ increases. This is likely a
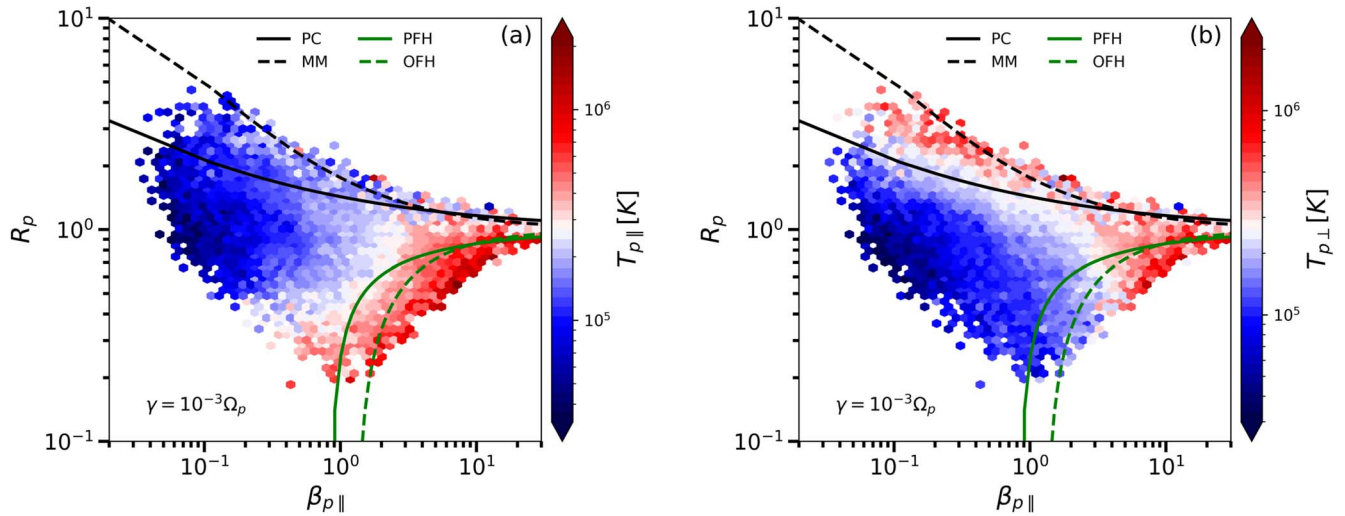
**Figure 3.** Plots of bin-median (a) $T_{p\parallel}$ and (b) $T_{p\perp}$ in the $(\beta_{p\parallel}, R_p)$ plane. The overplotted curves represent instability thresholds, as seen in Figure 2. The increase in the $T_p$ seen in Figure 2 is mainly in the parameter space beyond the PC and OFH thresholds. For $\beta_{p\parallel} > 2$, we also see significant enhancement in the $T_{p\perp}$ beyond the OFH instability threshold and the $T_{p\parallel}$ beyond the PC instability threshold.

consequence of anisotropy-driven instabilities, which arise when $R_p \neq 1$ (S. P. Gary 1993; P. H. Yoon 2017). The activated instabilities eventually drive the velocity distribution function toward isotropy by scattering particles in phase space on the growing electromagnetic fluctuations. We observe that for $R_p < 1$, the OFH instability thresholds mainly constrain the anisotropy, whereas for $R_p > 1$, the MM instability regulates the sheath plasma's anisotropy even at $\beta_{p\parallel} \leqslant 2$ (Z. I. Shaikh et al. 2023). The exact cause of this remains unknown despite various prior studies confirming it in the general solar wind— basically (P. Hellinger et al. 2006) and onward. However, it can be due to the following reasons: (1) MM instability is nonpropagating and thus potentially more efficient at scattering particles in phase space (D. J. Southwood & M. G. Kivelson 1993; S. D. Bale et al. 2009); (2) large-scale magnetic turbulence tends to align perpendicular to the background magnetic field, which accelerates the MM instability onset (F. Sahraoui et al. 2010; Y. Narita et al. 2011); and (3) deviations from the bi-Maxwellian assumption create a mismatch between the Vlasov–Maxwell prediction and the actual threshold.

The temperature in plasma unstable to PC and OFH instability is at least 7 to 10 times higher than the plasma stable to PC and OFH instability within ICME sheaths. We observe high median $T_p$ when $\beta_{p\parallel} \geqslant 2$, which is due to high median $T_{p\perp}$ when $T_{p\perp} > T_{p\parallel}$ and when $T_{p\perp} < T_{p\parallel}$. Our result is qualitatively but not quantitatively consistent with B. Maruca et al. (2011), who proposed that plasma unstable to mirror or firehose instability was 3 to 4 times hotter than stable plasma in the solar wind. The resonant heating and dissipation of kinetic Alfvén waves are proposed causes of anisotropic heating, whereas CGL double-adiabatic expansion predicts anisotropic cooling (G. Chew et al. 1956; E. Marsch & C.-Y. Tu 2001; B. D. Chandran et al. 2010). Our analysis shows that plasma unstable to cyclotron and OFH instabilities is significantly hotter than stable plasma in ICME sheaths. It is important to note that at any fixed beta, the trend in $T_p$ as a function of $R_p$ comes solely from $T_{p\perp}$. This means that, near that threshold, more energy is being pumped into the particles. This means that local heating pushes the plasma toward and beyond the thresholds in this regime. Most of the heating goes into $T_{p\parallel}$, but

there is also some going into $T_{p\perp}$, thus leading to the increased $T_p$ overall in this region. Our findings suggest that perpendicular heating is responsible for bringing the plasma close to or above the thresholds for the instabilities at $R_p > 1$. The plasma close to or above the thresholds for the instabilities at $R_p < 1$ also exhibits greater $T_{p\perp}$ than the neighboring plasma, suggesting that even stronger parallel heating occurs in these intervals to achieve $R_p < 1$. This observation suggests that parallel and perpendicular heating occur simultaneously but at different heating rates. Therefore, the timescale at which the adiabatic expansion and the compression of the sheath plasma occur is an important determining factor for enhancing the heating of the ICME sheath compared to the solar wind. It is likely that the compression of sheath plasma, which enhances magnetic fluctuations, occurs on a faster timescale compared to adiabatic expansion during the passage of an ICME, leading to the dominance of the heating processes. This results in net-enhanced heating compared to the regular solar wind.

We also observe high-amplitude magnetic fluctuations close to the region unstable to PC and PFH/OFH instabilities and low fluctuation close to $T_{p\perp} \sim T_\parallel$. This indicates that turbulence is important in maintaining anisotropic heating and cooling within the ICME sheath plasma. R. A. Qudsi et al. (2020) found indications that turbulence drives local anisotropic heating that ultimately pushes the plasma over the instability threshold. If the first adiabatic invariant is conserved, then a simple estimate of the pitch-angle scattering rate due to Alfvénic fluctuations gives $\nu = 1/T_{p\perp} dT_{p\perp}/dt \sim \omega_c \langle (\delta B_{\rm rms}/B_o)^2 \rangle$ (S. D. Bale et al. 2009), which drives the plasma toward the instability thresholds at a rate comparable to the solar wind expansion rate ($V_p/L$, where $L = 1\,{\rm au}$). If we assume the same is true in the case of ICME sheath, the achievement of instability requires $\langle \delta B_{\rm rms}/B_o \rangle \gtrsim (V_p/(\omega_c L))^{1/2} \sim 10^{-3}$, and the pitch-angle scattering should be fast enough to constrain the anisotropy. We observe $\langle \delta B_{\rm rms}/B_o \rangle \geqslant 10^{-1}$ in the region near the thresholds and unstable to PC/PFH instabilities and at the high $\beta_p$ region. It is consistent with the solar wind (S. D. Bale et al. 2009). Thus, the particle pitch-angle scattering seems fast enough to constrain the anisotropy within the ICME sheaths.

We find that collisions are important in maintaining isotropic plasma conditions within the ICME sheaths. Our finding is
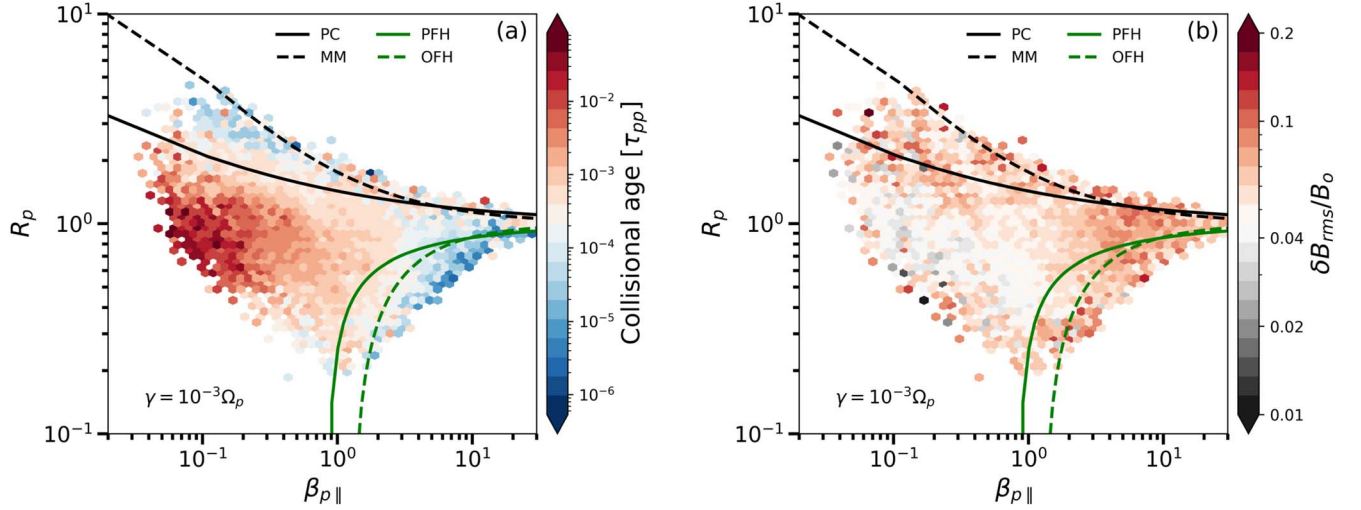
**Figure 4.** The plot of bin-median (a) "collisional age ($\tau_{pp}$)" and (b) magnetic fluctuation amplitude ($\delta B_{\rm rms}/B_o$) in the ($\beta_{p\parallel}$, $R_p$) plane. The $\tau_{pp}$ is highest around $R_p \sim 1$, suggesting that isotropy plasma derives largely from Coulomb collisions, whereas collisionless plasma is mostly anisotropic. The $\delta B_{\rm rms}/B_o$ shows enhancement in the vicinity of the instability thresholds at low $\beta_{p\parallel} < 2$ and at high $\beta_{p\parallel} > 2$.

consistent with earlier findings of the ambient collisionless solar wind, which suggest that more collisional plasma is more isotropic (J. Kasper et al. 2008; S. D. Bale et al. 2009; S. Vafin et al. 2019). This correlation applies to the expanding solar wind, where a positive correlation between temperature and proton speed and a negative correlation between proton temperature and density are observed (P. Hellinger & P. M. Trávníček 2014; C. Shi et al. 2023). However, in the case of an ICME sheath, the plasma (density, temperature, and magnetic field strength, etc.) does not vary significantly while traveling in interplanetary space until and unless it interacts with another ICME or corotating interaction region. Therefore, isotropization of plasma within ICME sheaths is likely to happen due to the fact that ICME sheath plasma is highly compressed (high density and enhanced plasma temperature compared to the ambient solar wind) and turbulent. We also observed a power-law dependence between proton temperature and collisional age as $T_p = 2.06 \times 10^4 \tau^{-0.3}$ (see the Figure in the Appendix material), suggesting that proton temperature and the collisional time have clear opposite behaviors, indicating an anticorrelation, which is similar to the ambient solar wind (P. Hellinger & P. M. Trávníček 2014).

ICME sheaths exhibit increased levels of fluctuations and higher densities, especially near the sheath onset and trailing edge of the ICME (W. Manchester IV et al. 2005; E. Kilpua et al. 2017; R.-Y. Kwon & A. Vourlidas 2018; C. Moissard et al. 2019; E. K. J. Kilpua et al. 2020; T. M. Salman et al. 2020). ICME sheaths present increased compressibility, lower magnetic power anisotropy, and a fluctuation power level that is approximately 10 times greater than in the preceding solar wind or the following ICME magnetic cloud (e.g., E. Kilpua et al. 2013; C. Moissard et al. 2019). Thus, the compressibility and high turbulent behavior could play an important role in the anisotropic enhancement of temperature (and its components) in the ICME sheath. As per the CGL double equations, $\frac{d}{dt}\left(\frac{P_\parallel B^2}{N^3}\right) = 0$ and $\frac{d}{dt}\left(\frac{P_\perp}{NB}\right) = 0$, where $N$, $B$, $P_\parallel$, and $P_\perp$ are number density, magnetic field strength, and parallel and perpendicular thermal pressure, respectively (G. Chew et al. 1956; P. Hunana et al. 2019). Thus, depending on how $N$ and $B$ change within the ICME sheath, this has different effects on the anisotropy. For example, if sheath plasma compresses slowly

and only $n$ changes and $B$ stays constant, then only $T_{p\perp}$ would change. A detailed investigation is needed to determine the role of compression in enhancing temperature (and its components) within the ICME sheath.

Recent statistical analysis suggests two types of ICME sheaths: planar sheaths (formed due to high compression) and nonplanar sheaths (E. Palmerio et al. 2016; Z. I. Shaikh et al. 2020). Plasma protons in planar sheaths have a significantly higher temperature than in nonplanar sheaths. In addition, Alfvénic fluctuations, turbulence, and reconnection processes are also observed within the ICME sheath region (Y. Liu et al. 2006; H. Li et al. 2017; Z. I. Shaikh et al. 2019a, 2019b; R. Marquez Rodriguez et al. 2023), which are potential candidates to explain the observed plasma heating. Our research is consistent with the predicted effect of these mechanisms on the temperature increase. The aforementioned processes may produce additional energy, leading to anisotropy development within the plasma system. A study of these processes and their impact on the anisotropy in the ICME sheath plasma is a worthwhile endeavor for future study.

## 4. Conclusion

Our study reveals that the threshold of MM and OFH instabilities mainly constrains anisotropy. We observe a notable increase in proton temperature (at least 7 to 10 times) within the parameter space that is unstable to PC and OFH instabilities. Our result differs from the solar wind finding (B. A. Maruca et al. 2012). The enhanced temperature is likely related to the high-amplitude magnetic fluctuations and low collisional age. The low collisional age is essential in allowing the anisotropy within ICME sheaths to persist.

## Acknowledgments

India. Moreover, this research was also supported by the International Space Science Institute (ISSI) in Bern, through ISSI International Team project #563 (Ion Kinetic Instabilities in the Solar Wind in Light of Parker Solar Probe and Solar Orbiter Observations) led by L. Ofman and L. Jian.

*Software:* MATLAB (https://in.mathworks.com/products/matlab.html), Python (NumPy, S. Van Der Walt et al. 2011; C. R. Harris et al. 2020; Matplotlib, J. Hunter 2007; Seaborn, M.L. Waskom 2021).

## Data Availability

We have utilized Wind spacecraft's data, which are publicly available at https://wind.nasa.gov/data.php, and Coordinated Data Analysis Web (CDAWeb), available at https://cdaweb.gsfc.nasa.gov/pub/data/wind/.

## Appendix A
## Limiting Anisotropy Distribution with Different Growth Rates ($\gamma$)

Figure 5 shows the median of $T_P$ per bin in the $(\beta_{p\parallel}, R_p)$ distribution plane, similar to Figure 2. The overplotted curves correspond to thresholds of different maximum growth rates such as $\gamma = 10^{-2}$ (solid), $\gamma = 10^{-3}$ (dashed), and $\gamma = 10^{-4}$ (dotted). The fitting coefficients $(a, b, \beta_0)$ in Equation (1) are determined from D. Verscharen et al. (2019). We can clearly observe that even at $\gamma = 10^{-2}$ (solid) and $\gamma = 10^{-4}$ (dotted), the plasma unstable to PC and firehose instabilities has higher temperatures than the stable plasma. The higher temperature in the case of $T_{p\perp} > T_{p\parallel}$ is mainly due to an increase in $T_{p\perp}$, whereas in the case of $T_{p\perp} > T_{p\parallel}$, it is due to enhancement in $T_{p\parallel}$ (figures are not shown here).



$\gamma = 10^{-2}\Omega_p(solid); \gamma = 10^{-3}\Omega_p(dashed); \gamma = 10^{-4}\Omega_p(dotted)$
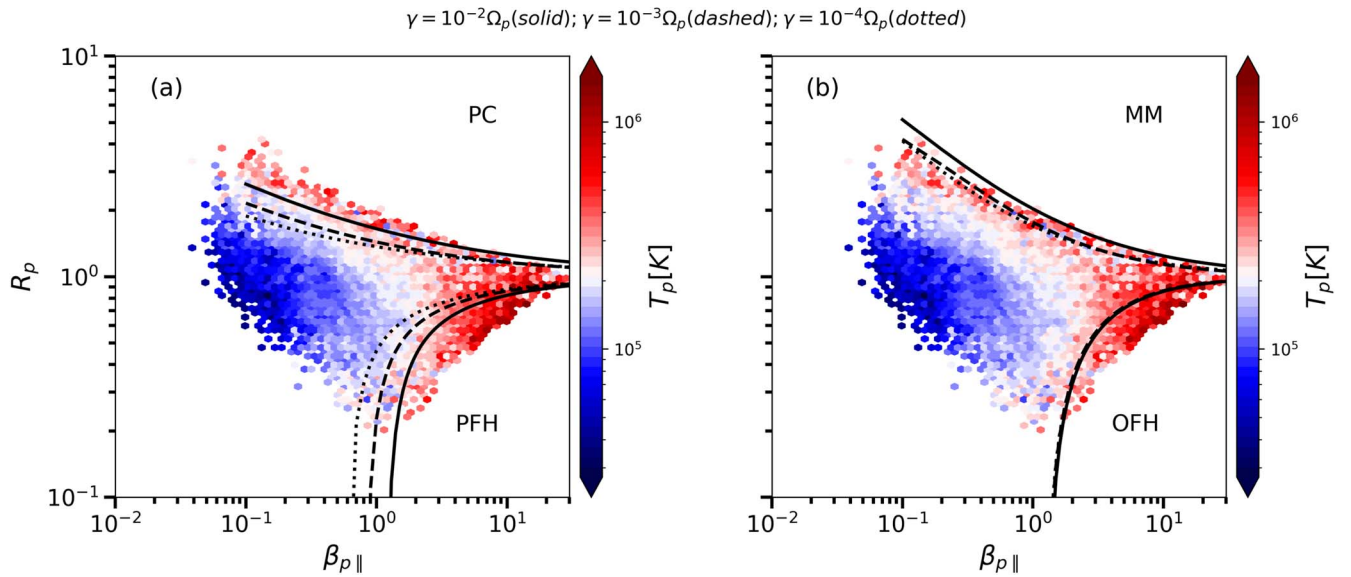
**Figure 5.** This is similar to Figure 2 but with different growth rate thresholds for PC, MM, PFH, and OFH instabilities.

## Appendix B
## Relation Between Proton Temperature ($T_p$) and Collisional Age ($\tau_{pp}$)

We used the Naval Research Laboratory (NRL) Plasma Formulary to estimate the collision frequency in a bi-Maxwellian plasma with no relative drift. This approach is approximative since it ignores relative drifts and secondary proton beams, which exist in the solar wind. The collisional relaxation of temperature anisotropy obeys (A. S. Richardson 2019; P. H. Yoon et al. 2024)

$$\frac{dT_{p\perp}}{dt} = \nu_{pp}(T_{p\parallel} - T_{p\perp}), \quad \text{(B1)}$$

$$\frac{dT_{p\parallel}}{dt} = 2\nu_{pp}(T_{p\perp} - T_{p\parallel}), \quad \text{(B2)}$$

where

$$\nu_{pp} = \frac{2\,\pi^{1/2}\,e^4\,N_p\,ln\Lambda}{m_p^{1/2}\,k_B^{3/2}\,T_{p\parallel}^{3/2}}F. \quad \text{(B3)}$$

$\nu_{pp}$, $m_p$, and $e$ are the Coulomb proton–proton collision frequency, proton mass, and electric charge unit, respectively. Moreover, $ln\Lambda$ is the Coulomb logarithm, given as

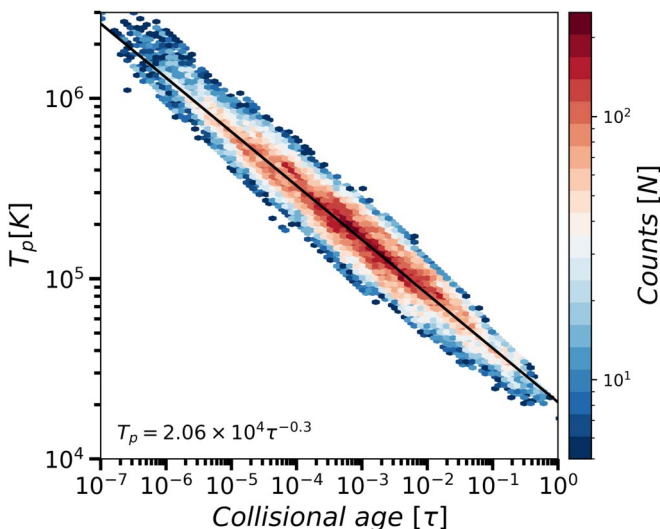$$ln\Lambda = 23 - ln\left[\frac{(2\,N_p)^{1/2}}{T_p^{3/2}}\right], \quad \text{(B4)}$$

and the quantity $F$ is given by

$$F = \frac{1}{A^2}\left[(A+3)\frac{\tan^{-1}\sqrt{A}}{\sqrt{A}} - 3\right] \quad \text{(B5)}$$

if $A > 0$ and

$$F = \frac{1}{A^2}\left[(A+3)\frac{\tanh^{-1}\sqrt{-A}}{\sqrt{-A}} - 3\right] \quad \text{(B6)}$$

if $A < 0$; here, $A = \frac{T_{p\perp}}{T_{p\parallel}} - 1$ (A. S. Richardson 2019). The collisional age $\tau = \nu_{pp}L/V_{sw}$ is a proxy for the number of collisional timescales that have elapsed during the plasma's

journey from the Sun to 1 au ($L/V_{sw}$, where $L$ is a distance of observed plasma parcel from the Sun (here it is 1 au) and $V_{sw}$ is the solar wind speed; S. D. Bale et al. 2009; P. Hellinger & P. M. Trávníček 2014). Figure 6 shows that the proton temperature and the collisional time are anticorrelated. A power-law fit to the observations in Figure 6 yields $T_p = 2.06 \times 10^4\tau^{-0.3}$. Equation (B3) suggests a direct temperature dependence of $\tau \sim T_p^{-3/2}$. Therefore, our weaker dependency of $\tau$ on $T_p$ suggests additional systematic interdependencies of the parameters entering our calculation of $\tau$.

## ORCID iDs

Zubair I. Shaikh https://orcid.org/0000-0002-9206-6327
Daniel Verscharen https://orcid.org/0000-0002-0497-1096
Ivan Y. Vasko https://orcid.org/0000-0002-4974-4786
Bennett A. Maruca https://orcid.org/0000-0002-2229-5618
Dibyendu Chakrabarty https://orcid.org/0000-0003-2693-5325
Anil N. Raghav https://orcid.org/0000-0002-4704-6706

## References

Ala-Lahti, M. M., Kilpua, E. K., Dimmock, A. P., et al. 2018, AnGeo, 36, 793
Bale, S. D., Kasper, J. C., Howes, G. G., et al. 2009, PhRvL, 103, 211101
Bothmer, V., & Daglis, I. A. 2007, Space Weather: Physics and Effects (Berlin: Springer)
Chandran, B. D., Li, B., Rogers, B. N., Quataert, E., & Germaschewski, K. 2010, ApJ, 720, 503
Chew, G., Goldberger, M., & Low, F. 1956, RSPSA, 236, 112
Cranmer, S. R., Field, G. B., & Kohl, J. L. 1999, ApJ, 518, 937
Gary, S. P. 1993, Theory of Space Plasma Microinstabilities No.7 (Cambridge: Cambridge Univ. Press)
Harris, C. R., Millman, K. J., Van Der Walt, S. J., et al. 2020, Natur, 585, 357
Hellinger, P., & Matsumoto, H. 2000, JGR, 105, 10519
Hellinger, P., Trávníček, P., Kasper, J. C., & Lazarus, A. J. 2006, GeoRL, 33, L09101
Hellinger, P., & Trávníček, P. M. 2008, JGRA, 113, A10109
Hellinger, P., & Trávníček, P. M. 2014, ApJL, 784, L15
Howes, G. G. 2010, MNRAS, 409, L104
Huang, J., Kasper, J. C., Vech, D., et al. 2020, ApJS, 246, 70
Hunana, P., Tenerani, A., Zank, G. P., et al. 2019, JPlPh, 85, 205850602
Hunter, J. 2007, CSE, 9, 90
Isenberg, P. A. 2001, JGR, 106, 29249
Kasper, J. C., Lazarus, A. J., & Gary, S. P. 2002, GeoRL, 29, 20
Kasper, J. C., Lazarus, A., & Gary, S. 2008, PhRvL, 101, 261103
Kilpua, E., Hietala, H., Koskinen, H., et al. 2013, AnGeo, 31, 1559
Kilpua, E., Koskinen, H. E., & Pulkkinen, T. I. 2017, LRSP, 14, 5
Kilpua, E. K. J., Fontaine, D., Good, S. W., et al. 2020, AnGeo, 38, 999
Klein, K. G., & Howes, G. G. 2015, PhPl, 22, 032903
Korreck, K., Zurbuchen, T., Lepri, S., & Raines, J. 2007, ApJ, 659, 773
Kwon, R.-Y., & Vourlidas, A. 2018, JSWSC, 8, A08
Lepping, R., Acuña, M., Burlaga, L., et al. 1995, SSRv, 71, 207
Li, H., Wang, C., Richardson, J. D., & Tu, C. 2017, ApJL, 851, L2
Liu, Y., Richardson, J., Belcher, J., Kasper, J., & Elliott, H. 2006, JGRA, 111, A01102
Luhmann, J. G., Gopalswamy, N., Jian, L. K., & Lugaz, N. 2020, SoPh, 295, 61
Manchester IV, W., Gombosi, T., De Zeeuw, D., et al. 2005, ApJ, 622, 1225
Marquez Rodriguez, R., Sorriso-Valvo, L., & Yordanova, E. 2023, SoPh, 298, 54
Marsch, E., & Tu, C.-Y. 2001, JGR, 106, 8357
Maruca, B., Kasper, J., & Bale, S. 2011, PhRvL, 107, 201101
Maruca, B. A., Chasapis, A., Gary, S. P., et al. 2018, ApJ, 866, 25
Maruca, B. A., Kasper, J. C., & Gary, S. P. 2012, ApJ, 748, 137
Matteini, L., Landi, S., Hellinger, P., et al. 2007, GeoRL, 34, L20105
Matteini, L., Landi, S., Hellinger, P., & Velli, M. 2006, JGRA, 111, A10101
Moissard, C., Fontaine, D., & Savoini, P. 2019, JGRA, 124, 8208
Murphy, N. A., Raymond, J., & Korreck, K. 2011, ApJ, 735, 17

**Figure 6.** The relative frequency of ($\tau$, $T_p$) occurrence. The overplotted black line denotes the power-law fitted curve.

Narita, Y., Gary, S. P., Saito, S., Glassmeier, K.-H., & Motschmann, U. 2011, GeoRL, 38, L05101

Ogilvie, K., Chornay, D., Fritzenreiter, R., et al. 1995, SSRv, 71, 55

Osman, K., Matthaeus, W., Hnat, B., & Chapman, S. 2012, PhRvL, 108, 261103

Palmerio, E., Kilpua, E. K. J., & Savani, N. P. 2016, AnGeo, 34, 313

Qudsi, R. A., Bandyopadhyay, R., Maruca, B. A., et al. 2020, ApJ, 895, 83

Raghav, A., Shaikh, Z., Bhaskar, A., Datar, G., & Vichare, G. 2017, SoPh, 292, 1

Raghav, A., Shaikh, Z., Vemareddy, P., et al. 2023, SoPh, 298, 64

Richardson, A. S. 2019, 2019 NRL Plasma Formulary (Washington, DC: Naval Research Laboratory)

Sahraoui, F., Goldstein, M., Robert, P., & Khotyaintsev, Y. V. 2009, PhRvL, 102, 231102

Sahraoui, F., Goldstein, M. L., Belmont, G., Canu, P., & Rezeau, L. 2010, PhRvL, 105, 131101

Salman, T. M., Lugaz, N., Farrugia, C. J., et al. 2020, ApJ, 904, 177

Schekochihin, A., Cowley, S., Dorland, W., et al. 2009, ApJS, 182, 310

Schwenn, R. 2006, LRSP, 3, 2

Seough, J., Yoon, P. H., Kim, K.-H., & Lee, D.-H. 2013, PhRvL, 110, 071103

Shaaban, S., Lazar, M., Poedts, S., & Elhanbaly, A. 2017, Ap&SS, 362, 1

Shaikh, Z. I., Raghav, A., & Vichare, G. 2019a, MNRAS, 490, 1638

Shaikh, Z. I., Raghav, A., Vichare, G., et al. 2019b, MNRAS, 490, 3440

Shaikh, Z. I., & Raghav, A. N. 2022, ApJ, 938, 146

Shaikh, Z. I., Raghav, A. N., & Vasko, I. Y. 2023, ApJL, 955, L5

Shaikh, Z. I., Raghav, A. N., Vichare, G., Bhaskar, A., & Mishra, W. 2018, ApJ, 866, 118

Shaikh, Z. I., Raghav, A. N., Vichare, G., Bhaskar, A., & Mishra, W. 2020, MNRAS, 494, 2498

Shi, C., Velli, M., Lionello, R., et al. 2023, ApJ, 944, 82

Southwood, D. J., & Kivelson, M. G. 1993, JGR, 98, 9181

Tu, C.-Y., & Marsch, E. 2001, JGR, 106, 8233

Vafin, S., Riazantseva, M., & Pohl, M. 2019, ApJL, 871, L11

Van Der Walt, S., Colbert, S. C., & Varoquaux, G. 2011, CSE, 13, 22

Verscharen, D., Bourouaine, S., & Chandran, B. D. 2013, ApJ, 773, 163

Verscharen, D., Klein, K. G., & Maruca, B. A. 2019, LRSP, 16, 5

Waskom, M. L. 2021, JOSS, 6, 3021

Webb, D. F., & Howard, T. A. 2012, LRSP, 9, 3

Yoon, P., Seough, J., Salem, C., & Klein, K. 2019, PhRvL, 123, 145101

Yoon, P. H. 2016, JGRA, 121, 10,665

Yoon, P. H. 2017, RvMPP, 1, 4

Yoon, P. H., Lazar, M., Salem, C., et al. 2024, ApJ, 969, 77

Yordanova, E., Voros, Z., Sorriso-Valvo, L., Dimmock, A. P., & Kilpua, E. 2021, ApJ, 921, 65

Zurbuchen, T. H., & Richardson, I. G. 2006, In-Situ Solar Wind and Magnetic Field Signatures of Interplanetary Coronal Mass Ejections (New York: Springer), 31